



# Optimization of Laminar Flow in Non-Circular Ducts: A Comprehensive CFD Analysis

Mohammed Hadi Hameed<sup>1</sup>, Hafidh Hassan Mohammed<sup>1</sup>, Mohammed Abdulridha Abbas<sup>2,3\*</sup>

<sup>1</sup> Mechanical Engineering Department, Faculty of Engineering, University of Kufa, 54003 Najaf, Iraq

<sup>2</sup> Aeronautical Techniques Engineering Department, Engineering Technical College-Najaf, Al-Furat Al-Awsat Technical University (ATU), 54001 Najaf, Iraq

<sup>3</sup> Sustainable Manufacturing and Recycling Technology, Advanced Manufacturing and Materials Center (SMART-AMMC), Universiti Tun Hussein Onn Malaysia (UTHM), 86400 Parit Raja, Malaysia

\* Correspondence: Mohammed Abdulridha Abbas ([mohd.a.abbas@atu.edu.iq](mailto:mohd.a.abbas@atu.edu.iq))

Received: 10-30-2023

Revised: 12-09-2023

Accepted: 12-17-2023

**Citation:** M.H. Hameed, H.H. Mohammed, M.A. Abbas, "Optimization of laminar flow in non-circular ducts: A comprehensive CFD analysis," *J. Sustain. Energy*, vol. 2, no. 4, pp. 175–196, 2023. <https://doi.org/10.56578/jse020402>.



© 2023 by the authors. Published by Acadlore Publishing Services Limited, Hong Kong. This article is available for free download and can be reused and cited, provided that the original published version is credited, under the CC BY 4.0 license.

**Abstract:** This study presents a detailed Computational fluid dynamics (CFD) analysis, focusing on optimizing laminar flow within non-circular ducts, specifically those with square, rectangular, and triangular configurations. The study centers on the effective use of mesh quality and size in these ducts, a factor which is previously underrepresented in those CFD studies that predominantly emphasized turbulent rather than laminar flows. With the help of finite element approach, this study compares the performance of these non-circular ducts, employing Reynolds numbers ranging from 1600 to 2000 and mesh sizes of 6, 12, and 18 mm. A ribbed duct style, arranged in a hybrid manner, is adopted to further this study. Analysis in this paper applied the Single predictive optimization (SPO) technique to the identification of the K- $\epsilon$ -Standard as the preferred viscosity model and a hybrid rib distribution as optimal within the triangular duct configuration. Parameters of a Reynolds number of 1600 and a mesh size of 18 mm emerged as the most effective values for this duct style. Then, the attained results of the Analysis of variance (ANOVA) indicated the F-Criterion's insignificance for Reynolds laminar levels, rendering the laminar viscosity model less relevant within the test section. Additionally, the implementation of the Six sigma procedure (SSP) markedly enhanced both the performance factor (PF) and turbulence intensity, which were observed at 4.90% and 146.77%, respectively. This improvement was most notable in the triangular duct, characterized by rib heights of 66 mm (semi-circle), 66 mm (rectangular), and 38.126 mm (triangular).

**Keywords:** Non-circular ducts; Laminar flow; Computational fluid dynamics (CFD); Mesh optimization; Single predictive optimization (SPO); Triangular duct; Ribbed duct style; Reynolds number; Analysis of variance (ANOVA); Six sigma procedure (SSP); Performance factor (PF)

## 1 Introduction

Numerous flow duct types have been exposed to different studies owing to the wide range of applications utilized in heat flow [1]. It also highlighted the influence of heat transmission in these ducts, where it has been dealt with both the passive and active mechanisms of this transmission. As it is known, the passive mechanism has been preferred in the flow duct since it generates swirls near the transferring surface and has little energy consumption compared to other types. Therefore, researchers have strived to enhance this field by adopting effective designs for the ducts [1, 2].

The geometric shape of the ducts is considered one of the most important determinants that affect flow and heat transfer, besides determining the force required for fluid flow through these ducts [3]. It was observed that entropy generation was a sign of flow quality when specifying the best style of duct shape. Therefore, circular and triangular ducts have better performance in entropy generation compared to square and rectangular ducts [4–6]. Also, the triangular duct has the lowest irreversible and coefficient of shape ratio [7], which means it creates the least amount of entropy and helps heat transfer grow more than other duct styles. This brief description of smooth duct performance has clarified entropy's role in the flow of these ducts. However, the researchers especially strived to enhance the heat flow of non-circular ducts by adding ribs [8, 9].

As a revolutionary solution, the ducts added ribs or grooves at any wall of the duct walls to generate vortices and boost boundary layers by improving the heat flow [10, 11]. This modification has contributed to raising the Nusselt (Nu) number level and skin friction coefficient. The main reason for this outcome was to separate the flow by ribs, reconfigure, and generate a secondary flow, which enhanced the fluid flow [12, 13]. Designally, ribs were divided into hybrid and identical, where hybrid ribs had better thermal efficiency than other types [14, 15]. In addition, it separated the flux and re-binding and improved the Nusselt number [16]. Subsequently, in calculating entropy, its value in rib ducts is less than that of smooth due to the increase in the heat transfer rate in the thermal system. On the other hand, rib ducts have a better PF than smooth ones [17]. Accordingly, the role of hybrid ribbed tubes in the thermal transfer process is clear compared to other cases of ducts.

In smooth and ribbed ducts, the performance of heat flow was diverse depending on the Reynolds (Re) number level. In other words, the laminar, transient, and turbulent flow behaviors in these ducts have been reported by prior studies depending on this number [18, 19]. In the early studies, the heat flow of non-circular smooth ducts was gradient at  $1000 \leq Re \leq 2000$  and tended to be stable [5–7]. In the same way, the Re number has significantly influenced energy loss as the growth of this number induced the wall temperature to drop [13]. Similarly, as the Reynolds number advances, the Nu number rises, and the skin friction factor decreases. Hence, this is due to the growth in turbulence in the flow [16]. The consequence of laminar flow in the smooth ducts has simultaneously reduced the heat transfer rate and coefficient of friction for non-circular tubes compared to circular ones, while in turbulent flow, the values were almost equal [20]. Besides, the ribs led to the separation of the flow and the formation of a stagnation zone, which caused a decrease in the Nu number. Therefore, a rise in the Re number caused a decrease in this region and improved the local Nu number due to an augmentation in this number [21, 22]. By essential, these brief outcomes referred to the performance of the flow duct being differentiated when the Re number approximated over 1000. Moreover, these performance levels were consistently very close at  $Re = 2000$ .

These results show that mesh quality and element size were two more factors that affected how well the CFD analysis predicted the design of the heat flow duct in tubes. Unfortunately, numerous studies in this field have not highlighted the mesh intensity based on the finite element method (FEM) and have not deepened interest in these factors [23, 24]. Wherein mesh size is essential for confining the accuracy of the outcomes and computational time for simulation [25, 26]. One of the momentous studies has explored the dominant role of mesh besides the numbers Nu and Re in specifying the efficient flow in rectangular ducts [27]. Additionally, it was noted that the flow velocity in this type of duct was affected by increasing mesh size. This increase has contributed to the growth of the boundary layers of the smooth walls [28]. On the other hand, the variance of mesh intensity played a considerable role in specifying the finest predictive value of heat flow in the triangular duct [29]. Based on these outcomes achieved, the size, intensity, and quality of the mesh were powerful factors in picking the successful path of CFD prediction.

Based on the results of this short survey, there seems to be a strong connection between the type of ducts, the amount of flow, and the size of the mesh elements. These factors have a big effect on how well CFD can predict the heat transfer of airflow in non-circular ribbed ducts. Unfortunately, the previous study did not profoundly present a comparison study of this type of performance and proposed methods to enhance these kinds of ducts depending on the statistical analysis and the optimization techniques. Accordingly, the primary objective of the current work is to employ these parameters to determine the optimum prediction for heat flow in these ribbed ducts. Therefore, the present study used square, rectangular, and triangular tubes as a flow style. Besides, the flow levels in these ducts ranged from 1600–2000 for the Reynolds number, while the mesh sizes employed in the simulation were 6, 12, and 18 mm. Furthermore, the hybrid ribbed style was adopted in these ducts, where it was sequentially arranged as half-circular, triangular, and rectangular at a height of 30 mm for each rib. The best output from this stage of the SPO method helps test the viscosity model, the distribution of ribs, and the height levels of each rib to find out which of these ribbed ducts has the best thermal performance.

From the preceding, it is essential to comprehend the methodology of this study, which is organized into the style of airflow ducts, the description of the duct environment, mesh quality, and the SPO technique.

## 2 Methodology of CFD Simulation

It turns out that the simulation operation by CFD has a considerable role in predicting the influential design of ribbed ducts, as aforementioned in the brief survey. To understand the laminar flow behavior in the rectangular, square, and triangular shapes of these tubes, the CFD method was used as a significant prediction environment. To find the best way to move heat in this case using a computer simulation system that is very accurate, the pattern of hybrid ribbed ducts (HRDs) has been planned for this study. So the commercial ANSYS software has been employed to implement the 3D modeling of HRDs and simulate these ducts. Hence, the hypotheses considered to achieve the present work were:

- (1) The laminar flow mechanism embraces an untransient mode and incompressible flow [30].
- (2) Along the rectangular, square, and triangular ducts, the merits of fluid are regular. Hence, the air is employed in these ducts as a fluid domain [31, 32]. As demonstrated in Table 1, it can recognize the air properties at 300 K

[33].

(3)The condition of an interface between fluid and the structure of ducts is no-slip [34, 35].

**Table 1.** Thermo-physical properties of air flow at 300 [33]

Thermo-Physical Properties	Unit	Value
Thermal conductivity ( $k$ )	W/m.K	0.025
Density ( $\rho$ )	kg/m <sup>3</sup>	1.176
Dynamic viscosity ( $\mu$ )	kg/m · s	$186 \times 10^{-6}$
Specific heat capacity ( $C_p$ )	g.K	1007

## 2.1 Style of Airflow Ducts

After going through the objectives of the current article, it is crucial to model the ribbed ducts as the first step of the planned methodology. Therefore, all tube models were ribbed as grooves to enhance thermal performance, where the ribs were designed, as demonstrated in Figure 1, in a hybrid manner in these ducts to semi-circle, triangular, and rectangular grooves [14]. Furthermore, these tubes have been classified into square, rectangular, and triangular to investigate if the triangular ribbed ducts are best, besides comparing one of the close studies to validate the optimal case [36–38].

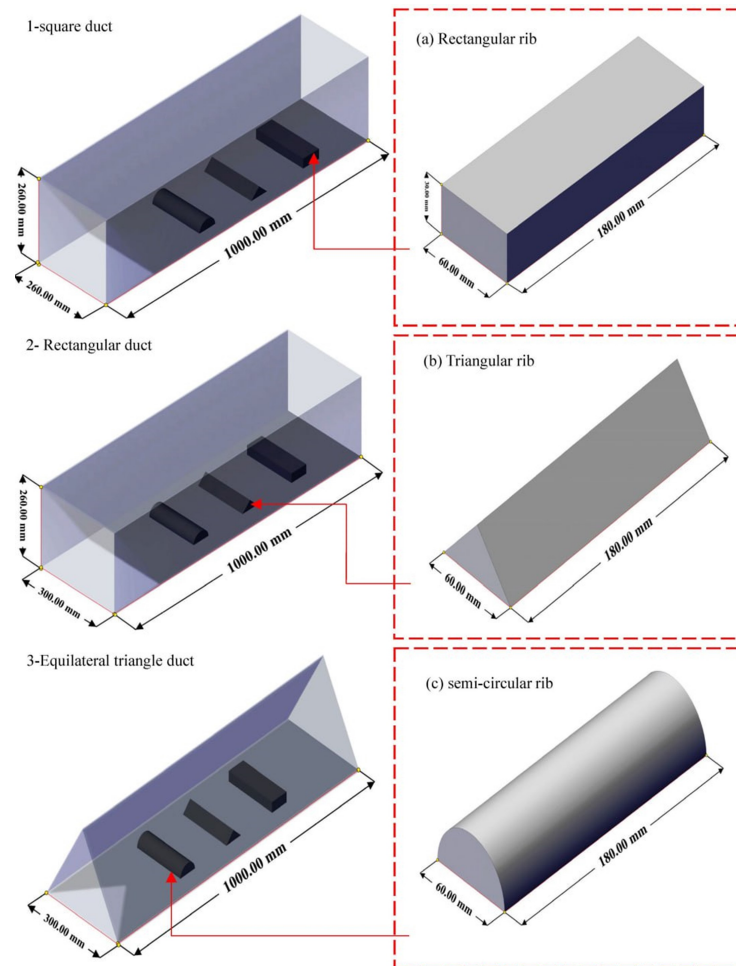


**Figure 1.** Schematic of ducts styles: (1) Square duct, (2) Rectangular duct, and (3) Equilateral triangle duct. Observed ribs configuration: (a) Rectangular, (b) Triangular, and (c) Semi-Circular

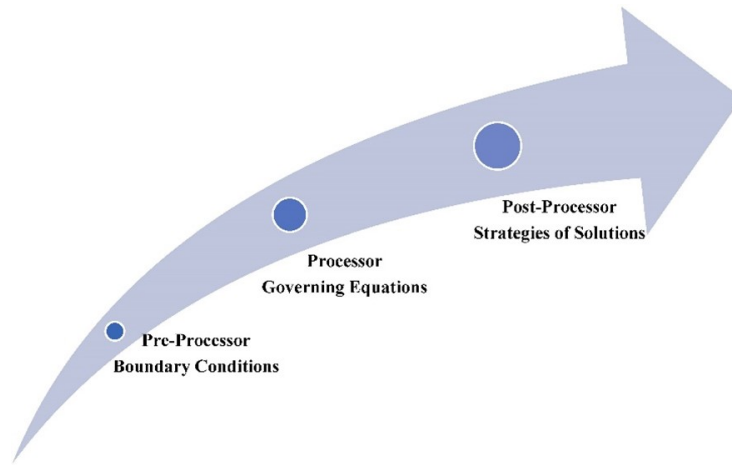
Remarkably, the details of dimensions are depicted in Figure 1 for each ribbed duct, where it was assigned to simulate the numerical analysis based on CFD principles to predict the optimal case. In turn, each tube has been split into an entrance zone and a fully developed region, as illustrated in Table 2. Hence, the grooved side is heated using a steady amount of heat flux at  $450 \text{ W/m}^2$  and exposed to the constant velocity at levels 1600, 1800, and 2000 of the Re number.

**Table 2.** Dimensions of entrance and fully developed regions in each flow duct

Sections	Entrance Zone Characteristic Length Section (mm)	Fully Developed Region Ribbed Section (Test Section) (mm)	Exit Section (mm)
Square duct	260	456	284
Rectangular duct	278	456	266
Equilateral triangular duct	173	456	371
Distance between ribs centers (mm) [14]		189	
Total length duct (mm) [38]		1000	

## 2.2 Environment of Numerical Flow

The selection of one of the proposed ducts, as exemplified in Figure 1, is observably deemed the main path of this study. Hence, the numerical solution using FEA based on CFD principles is a basis for achieving this path. Therefore, the boundary conditions, governing equations, and techniques of the solution represent the pre-processor, processor, and post-processor steps, respectively, as depicted in Figure 2. Accordingly, the highlights of these steps contribute to comprehending the role of each stage in the numerical environment.

**Figure 2.** Steps of numerical environment

### 2.2.1 Pre-processor step

According to the adopted hypotheses in the current work, it becomes clear that the flow of air in present HRDs varies based on Re numbers. Wherein these numbers contribute to variance in the inlet velocities at each type of duct, as illustrated in Figure 1. These velocities result in the removal of heat from the heated surface, particularly in the rib-stimulated zone, where this zone increases the heat away from the laminar flow mechanism. As a result of this behavior, the walls of unribbed sides did not interact with this heat transfer state and behaved as adiabatic walls. On the other hand, the outlet zone is designed to be under atmospheric pressure. Thus, after describing the outlines of boundary conditions utilized in this study, it is vital to exhibit the data on these boundaries, as demonstrated in Table 3.

**Table 3.** Boundary conditions of HRDs

Name of the Boundary	Assigned Condition	Value
Domain inlet [5–7, 21, 22]	Reynolds number (Re)	1600, 1800 and 2000
Domain outlet	Pressure	101.325kPa
Base of the duct	Heat flux	450 W/m <sup>2</sup>
Unribbed walls	Adiabatic wall	No-Slip condition

### 2.2.2 Processor step

The continuity, momentum, and energy models are considered a well-trodden path for processing the domain toward the solution in the CFD technique. The researchers have followed this path in almost all HVAC applications

to describe the fluids' dynamic and computation processes. From here, these models were employed under the steady state and laminar conditions in the ducts illustrated in Figure 1, depending on the hypotheses adopted in the present study. Hence, these models can be written as follows, based on the Cartesian coordinate system [39, 40]:

Continuity model:

$$\frac{\partial u}{\partial x} + \frac{\partial v}{\partial y} + \frac{\partial w}{\partial z} = 0, \quad (1)$$

Momentum model in x-direction:

$$u \frac{\partial u}{\partial x} + v \frac{\partial u}{\partial y} + w \frac{\partial u}{\partial z} = \nu \left\{ \frac{\partial^2 u}{\partial x^2} + \frac{\partial^2 u}{\partial y^2} + \frac{\partial^2 u}{\partial z^2} \right\} - \frac{1}{\rho} \frac{\partial P}{\partial x}, \quad (2)$$

Momentum model in y-direction:

$$u \frac{\partial v}{\partial x} + v \frac{\partial v}{\partial y} + w \frac{\partial v}{\partial z} = \nu \left\{ \frac{\partial^2 v}{\partial x^2} + \frac{\partial^2 v}{\partial y^2} + \frac{\partial^2 v}{\partial z^2} \right\} - \frac{1}{\rho} \frac{\partial P}{\partial y}, \quad (3)$$

Momentum model in z-direction:

$$u \frac{\partial w}{\partial x} + v \frac{\partial w}{\partial y} + w \frac{\partial w}{\partial z} = \nu \left\{ \frac{\partial^2 w}{\partial x^2} + \frac{\partial^2 w}{\partial y^2} + \frac{\partial^2 w}{\partial z^2} \right\} - \frac{1}{\rho} \frac{\partial P}{\partial z}, \quad (4)$$

Here, Newton's rule of motion produces Eqs. (2)-(4) for the flow toward x, y, and z, where these equations determined the momentum models of airflow in HRDs described in Figure 1.

$$u \frac{\partial T}{\partial x} + v \frac{\partial T}{\partial y} + w \frac{\partial T}{\partial z} = \alpha \left\{ \frac{\partial^2 T}{\partial x^2} + \frac{\partial^2 T}{\partial y^2} + \frac{\partial^2 T}{\partial z^2} \right\}, \quad (5)$$

where x, y, and z are the coordinate system, u, v, and w are the velocity vectors of airflow in the direction of the coordinate system, T indicates temperature,  $\nu$  is the kinematic viscosity of air, P is the pressure,  $\alpha$  is the thermal diffusivity of airflow, and  $\rho$  is the airflow density. Besides the models describing viscosity, energy, and continuity as governing equations in the domain process of flow, it is vital to comprehend these models depending on CFD to obtain the final destination of the prediction of the optimal solution. Therefore, to reach this destination, it is significant to emphasize the strategies of the solution followed in CFD.

### 2.2.3 Post-processor step

As aforementioned, the steps of the pre-processor and processor have indicated the boundary conditions and the governing equations for energy, momentum, and continuity consecutively. Here, these steps paved the way for the strategies of solutions as a post-processor step in the numerical environment for the depicted ducts in Figure 1, implemented by the segregated technique.

As is famous in the CFD field, this technique simultaneously treats the equations of velocity and pressure. Hence, the solution for the segregated path has been adopted here as one of the active and public algorithms known as the Semi-Implicit Method for Pressure-Linked Equations (SIMPLE) algorithm [41]. This algorithm contributes to solving the governing equations in the incompressible flow case. Moreover, this algorithm accurately employed the scheme upwind with a second order. Concerning spatial estimation, the method Green-Gauss Node Based for the gradient was adopted with this algorithm. On the other hand, the convergence criteria for the solutions of governing equations are designated at 10E-06 and 10E-03 for the energy equation and velocity components, respectively. The main reason this convergence limit was chosen for the speed parts is to keep the total shear stress from acting in a straight line at the boundary layers [42]. The large mesh size also cuts down on the time it takes to find a solution by lowering the normalized residuals for the logarithm used in the finite volume analysis at 10E-03 for the velocity components. On the other hand, the Nusselt number suffers from an unstable solution for these components when the convergence limits range from 10E-4 to 10E-06 at  $< 4$  m/s for inlet velocity. After that, this algorithm's answer is stable from 500 to the transient mode of flow levels based on the Reynolds formula for the laminar and k- $\epsilon$  models at 10E-03 [43, 44]. This means that the results of normalized residuals for the logarithm are stable at 10E-03 if, depending on the mesh size [45], the number of tangential velocity distributions in the flow is higher than the number of repetitions of tangential velocity at the duct. However, the convergence of energy criterion at 10E-06 can be used



instead of 10E-03, as the laminar viscosity model cannot overcome the boundary layer at the entrance region. After that, the correct answer to the created unsteady governing differential equation for the energy criterion causes flow confusion at the ribbed section, which leads to the solution becoming less consistent. Accordingly, the temperature components of this governing equation at 10E-06 pretty much lessen this unstable convergence [46].

According to this context, the steps of the numerical environment in Figure 2 for the flow domain have been described, which is used in this study. However, it is necessary to highlight the divided elements of this environment besides the mesh efficiency based on the quality criteria followed at each ribbed duct.

### 2.3 Mesh Quality

The FEM is one of the best numerical tools utilized in CFD solutions. On top of that, it was carefully aligned to the finite element volume (FEV) procedure path as a tool used in the ANSYS-FLUENT traditional program to manage the numerical environment and pick the mesh quality that works best [47–49]. At this juncture, the skewness quality criterion is one of the best criteria to choose the best quality when the maximum value of this criterion approaches zero [50, 51]. Unfortunately, the previous studies were not meaningfully focused on obtaining the best mesh quality for the gridded airflow domain in ribbed ducts [52–54]. Consequently, the current work has employed a mesh size factor at each non-circular ribbed duct to specify the efficient quality. Moreover, the present work has utilized similar CFD cases that used mesh size in the flow ducts since there were a few studies that dealt with the role of the size of mesh elements in this field, as illustrated in Table 4:

**Table 4.** Mesh sizes adopted in the previous studies

Reference No.	Element Sizes (mm)	Duct Length (mm)
[55]	0.2, 0.25, 0.5, 0.75, 1	150
[56]	0.6, 0.8, 1, 2, 3, 4, 5	4D
[57]	20 to 100	> 3000

Note: D is Duct diameter

The mesh size data in Table 4 makes it clear that the element size is smaller for short tubes and bigger for longer tubes. This allows for more flexibility in how the CPU unit handles the convergence time [55]. Furthermore, the tube length in the present work did not exceed 1 m. Therefore, it is reasonable to use the options in Table 4 to conclude that ( $2 \text{ mm} < \text{element size} \leq 20 \text{ mm}$ ) is more suitable for our tube length. The main reason for this choice is that the finer mesh is more logical for smaller tube sizes [56]. On the other hand, the minimum mesh size limit adopted at over 3 m was 20 mm [57]. To choose the best quality of the gridded domain at each duct, as shown in Figure 1, elements with sizes ranging from 4 to 20 mm were tested to find the most important quality based on the skewness criterion. The tested elements in the square, triangular, and rectangular ribbed ducts have success at 6, 12, and 18 mm. Whereby it tended to reach toward the zeroth value, as demonstrated in Figure 3, depending on the maximum criterion of skewness. Additionally, it is observed in Figure 3 that the best mesh quality is concentrated at the coarse mesh [28]. Still, these three values are essential to the planned optimized path to finally select the best-meshed domain in the last predictive solution.

### 2.4 SPO Procedure

The significant parameters always nurture the optimization path to obtain the desired destinations as final responses. Hence, this trend contributed to enhancing the performance of ribbed ducts and boosting heat transfer [58]. Therefore, SPO is deemed one of the most popular and paramount optimization techniques used in diverse engineering areas, depending on the basic factorial optimization [59, 60]. Hence, this optimization technique requires determining the influential parameters to predict the efficient performance of the HRD system adopted in the present work.

The range of effective values of Re numbers in the laminar flow has been found in the designated ducts shown in Figure 1 so that the planned comparison operation in this study can be carried out, as was already said. In addition, the mesh quality grades of the flow domain were described in Figure 3 based on the comparison with the mesh size. Thus, it has become evident, as illustrated in Table 5, the scope adopted in the SPO technique to implement factorial path optimization. This scope was designed to accomplish the number of simulation runs needed to predict the optimum case. So, the PF is the last result of the SPO method. It shows how well the airflow system works thermally, based on how much the pressure drop at each ribbed duct grows. Hence, this factor at each simulation run can be calculated as follows [61–63]:

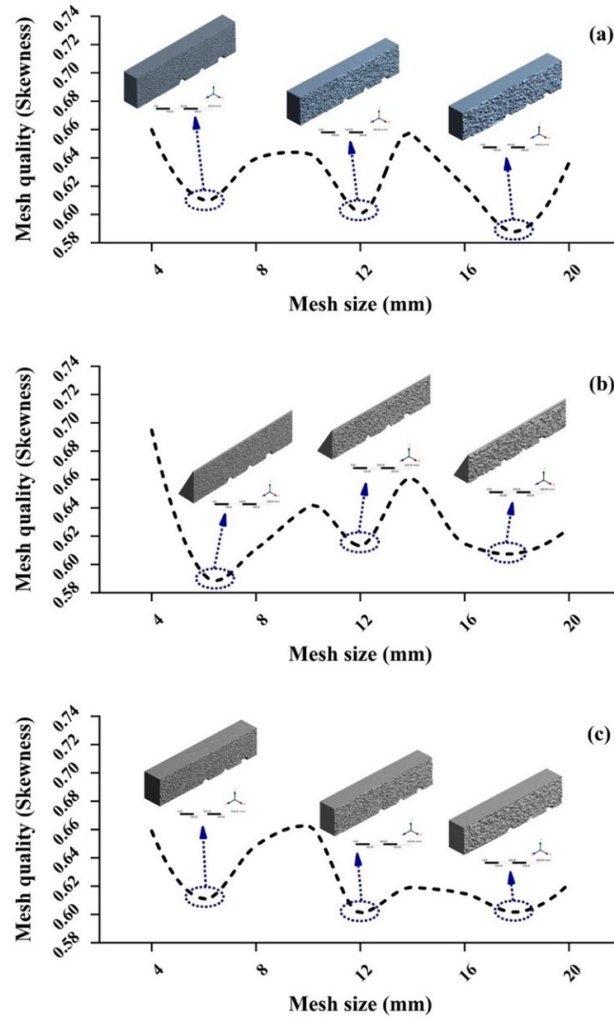


**Figure 3.** Variance mesh quality based on mesh size. Observed in: (a) Square ribbed duct; (b) Triangular ribbed duct; (c) Rectangular ribbed duct

**Table 5.** Levels of parameters applied in SPO

Parameter	Symbol	Levels		
		- 1	0	1
Mesh size (mm)	A	6	12	18
Reynolds number (Re)	B	1600	1800	2000
Duct type	C	Square (Sq)	Rectangle (Re)	Triangle (Tr)

$$PF = \left( \frac{Nu}{Nu_i} \right) \left( \frac{S_f}{S_i} \right), \quad (6)$$

$$Nu = \frac{hD}{k}, \quad (7)$$

$$Nu_i = 0.023 Re^{0.8} Pr^{0.4}, \quad (8)$$

$$Re = \frac{\rho D u_i}{\mu}, \quad (9)$$

$$S_f = \left( \frac{\Delta P}{2\rho} \right) \left( \frac{D}{lu_i^2} \right), \quad (10)$$

$$S_i = (1.58 \ln Re - 3.28)^{-2}, \quad (11)$$

where  $Nu$  and  $Nu_i$  are the dimensionless's Nusselt numbers at ribbed and un-ribbed ducts, sequentially,  $S_f$  and  $S_i$  denote friction factors for the test section in a fully developed zone and smooth duct, respectively,  $h$  is the heat transfer coefficient for airflow,  $Pr$  is a dimensionless's Prandtl number,  $u_j$  is inlet velocity at each ribbed non-circular duct type,  $\mu$  is the dynamic viscosity of airflow,  $\Delta P$  is the drop pressure in the test section, and  $l$  is the test section length. According to Eqs. (6)–(11), the  $PF$  was reported in Table 6 at each simulation run. Moreover, the final formula of this factor is identified, as revealed in Eqs. (12) and (13) by polynomial expressions depending on the parameters and outcomes in Table 6 [64, 65].

$$R = G^P, \quad (12)$$

$$PF = a_o + \sum_{i=1}^n a_i A_i + \sum_{j=1}^n a_j B_j + \sum_{k=1}^n a_k C_k + \sum_{i=1}^n \sum_{j=1}^n a_{ij} A_i B_j + \sum_{i=1}^n \sum_{k=1}^n a_{ik} A_i C_k + \sum_{j=1}^n \sum_{k=1}^n a_{jk} B_j C_k, \quad (13)$$

**Table 6.** Number of runs designed and outcomes of PF

Run No.	Parameters			Response	RES	FIT
	Mesh Size (mm) (A)	Reynolds Number (B)	Duct Type (C)	Performance Factor (PF)		
1	6	1600	Sq	0.9112	0.0038150	0.90737
2	6	1600	Re	1.0237	0.0060123	1.01768
3	6	1600	Tr	1.1651	-0.0098273	1.17497
4	6	1800	Sq	0.8891	-0.0001321	0.88925
5	6	1800	Re	0.9970	-0.0000081	0.99702
6	6	1800	Tr	1.1482	0.0001403	1.14804
7	6	2000	Sq	0.8712	-0.0036828	0.87491
8	6	2000	Re	0.9755	-0.0060041	0.98146
9	6	2000	Tr	1.1374	0.0096870	1.12774
10	12	1600	Sq	1.2232	0.0020353	1.22117
11	12	1600	Re	1.2413	-0.0020350	1.24330
12	12	1600	Tr	1.4790	-0.0000003	1.47904
13	12	1800	Sq	1.2102	-0.0000061	1.21021
14	12	1800	Re	1.2299	0.0000752	1.22978
15	12	1800	Tr	1.4592	-0.0000690	1.45926
16	12	2000	Sq	1.1975	-0.0020291	1.19951
17	12	2000	Tr	1.2198	0.0019599	1.21787
18	12	2000	Sq	1.4427	0.0000693	1.44261
19	18	1600	Re	1.4170	-0.0058503	1.42287
20	18	1600	Tr	1.5386	-0.0039773	1.54257
21	18	1600	Sq	1.7184	0.0098275	1.70854
22	18	1800	Sq	1.3835	0.0001383	1.38340
23	18	1800	Re	1.5005	-0.0000670	1.50056
24	18	1800	Tr	1.6602	-0.0000713	1.66026
25	18	2000	Sq	1.3520	0.0057120	1.34633
26	18	2000	Re	1.4663	0.0040443	1.46227
27	18	2000	Tr	1.6075	-0.0097563	1.61724

Note: RES is residual between PF and fit values; FIT is fitting of PF values



where  $R$ ,  $G$ , and  $P$  are the number of simulation runs, number of parameters' levels, and number of parameters, respectively. Furthermore,  $a_i$ ,  $a_j$ ,  $a_k$ ,  $a_{ij}$ ,  $a_{ik}$ , and  $a_{ijk}$  are regression coefficients, and  $A_i$ ,  $B_i$ , and  $C_k$  indicate mesh size,  $Re$  number, and duct type consecutively. The larger-is-better (LB) was adopted in the current study for PF response as a significant criterion for SPO of the desirability function. Thus, the statistical analysis and SPO implementation are accomplished utilizing Minitab 18, which is traditional statistical software. Consequently, the value of this function for the PF in the single destination can be described as follows [66–69]:

$$D = \begin{cases} 0 & PF_n < PF_L \\ \left( \frac{PF_n - PF_L}{PF_T - PF_L} \right)^{f_w} & PF_L \leq PF \leq PF_T, \\ 1 & PF_n > PF_T \end{cases} \quad (14)$$

where  $D$  is the final desirability of the  $PF$  response,  $PF_n$  is the desired  $PF$ , and  $PF_L$  and  $PF_T$  are the lower limits of the desired  $PF$  and targeted  $PF$ , respectively. Furthermore,  $f_w$  is the weight factor and equals one. This succinct description has introduced the whole notion of the SPO technique tracked in the present article. Therefore, the context of the current scenario adopted in this work has been scheduled to predict the optimum case of airflow in the HRD system first. Then, the second stage of this scenario is planned to investigate a studied case somewhat similar to this predictive case based on the viscous models and compare both cases based on rib style. This comparison aims to boost the PF of the optimum predictive case, depending on the distribution of ribs and the best viscous model. Finally, this case is improved by increasing the ribs' height to develop the PF of heat transfer for the optimum ribbed duct utilizing the SSP [70]. The flow chart in Figure 4 briefly reveals the planned progression at each stage to execute the methodology of the present study.

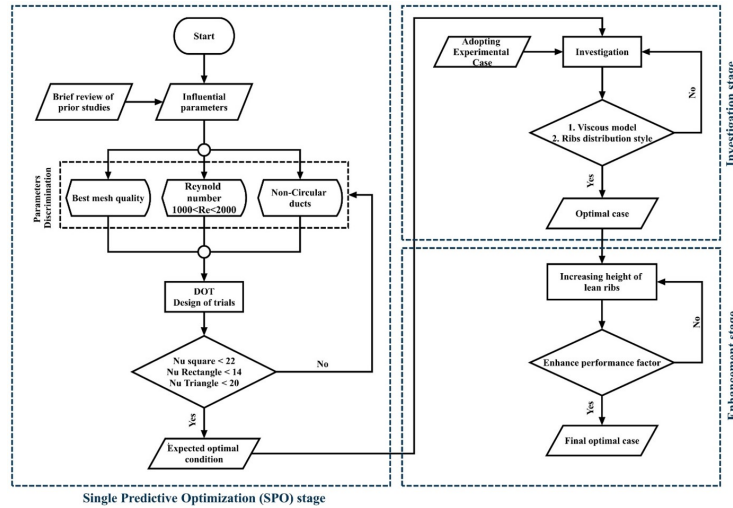


**Figure 4.** Flowchart of methodology progression stages

### 3 Results and Discussion

As described in Figure 4, the methodology of the present work was divided into three stages: single predictive optimization, investigation stage, and enhancement stage for the airflow of HRDs. Therefore, it is essential to highlight the contribution of each phase in boosting the final style of the duct and the role of the hybrid rib style in improving the heat distribution operation.

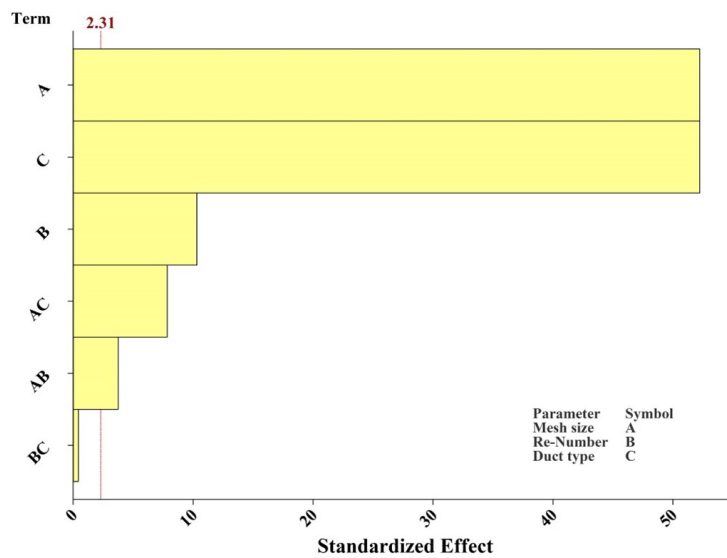
#### 3.1 Outcomes of SPO Stage

As a result of statistical behavior, the P-Values and F-Values for mesh size (A), Re-Number (B), and type of duct (C) show which parameters are important and which are not important in this study based on the ANOVA [71–73]. The final results of each simulation run represented by the PF response in Table 6 are inputted into the statistical analysis based on regression and ANOVA, where FIT and RES for this response are observed in Table 6 as poly-fit and residual values, respectively. Hence, the active values of RES for PF response are (-0.003682-0.009828) for runs 7 and 21 sequentially. One of these values, depending on the criteria of the SPO technique, is considered an optimal case.

**Table 7.** ANOVA for parameters employed in HRDs

Source	DF	Adj SS	Adj MS	F-Value	P-Value
Model	18	1.49397	0.082998	1110.64	0.000
Linear	6	1.48136	0.246893	3303.79	0.000
A	2	1.14549	0.572746	7664.18	0.000
B	2	0.01115	0.005574	74.59	0.000
C	2	0.32472	0.162360	2172.61	0.000
Interactions	12	0.01261	0.001051	14.06	0.000
A × B	4	0.00254	0.000635	8.49	0.006
A × C	4	0.00989	0.002473	33.10	0.000
Error	4	0.00018	0.000045	0.60	
Total	8	0.00060	0.000075		

Note: DF is degree of freedom; Adj SS is the summation of squares to adjust the account for variation in factor within the model; Adj MS is factor variation in the model adjusted by mean squares; F-Value is indicator to specify the essential values in ANOVA based on the greatest value of the standard ratio; P-Value is indicator to specify the significant values ranging ( $0 < P\text{-Value} < 0.05$ ) in ANOVA.

**Figure 5.** Standardized effect of HRDs parameters based on Pareto's chart

The dominant parameter in ANOVA and Pareto's chart in Table 7 and Figure 5, respectively, is mesh size. This parameter is deemed the first predominant factor in the numerical simulation of HRDs in the current work, where the P-value is zero, as demonstrated in Table 7, and the F-value of this parameter is 7664.18 [74, 75]. Hence, the outcome of the F-value in ANOVA for mesh size was compliant with Pareto's chart of standardized effect in Figure 5. Not only that, but this result fits with what we know about how the mesh resolution affects the flow in the ribbed duct [76]. At the same time, both duct type and Reynolds number in Table 7 and Figure 5 were ranked second and third, respectively. According to this analysis, the duct type in the CFD simulation based on the hydraulic diameter of the cross-sectional duct illustrated in Figure 1 is also a significant parameter to enhance the skin friction in the flow duct [4–7]. The linear behavior demonstrated in Table 7 for Reynolds number was also slightly influential compared to mesh size and duct type. The main reason for this behavior is attributed to the change in the airflow mechanism and the turbulent flow in the test section [77, 78]. Accordingly, the linear behavior role of these parameters based on ANOVA outcomes has been clarified. But it's important to know how the parameters that interact in ANOVA cause the regression model to behave in a way that isn't linear, as shown in Table 7 and Figure 1.

The F-value in the ANOVA shows that the mesh size and Reynolds number (A×B) were less important than the duct type (A×C) when looking at how they interacted in Table 7. This outcome means the duct type plays a substantial role in the ribbed duct, depending on the shape of the hydraulic diameter, in enhancing the stability of the heat transition and balancing the pressure drop in the entrance region. Besides, the shear stress at the wall depends on the mesh density to specify this stable behavior [79, 80]. However, the interaction of mesh size with Reynolds number, as depicted in Figure 6, refers to laminar flow being more stable at 1600 and 18 mm for Reynolds number and mesh size, respectively. So, the first result for SPO from ANOVA shows that the mesh size and Reynolds number tend to be the most accurate predictors without specifying the type of duct. In addition, the interaction between

Reynolds number and duct type is not influential since the P-value in the ANOVA of the current work is higher than 5% [64–69]. This interacted behavior is also inactive since the least hydraulic diameter employed reduces Reynolds number. This behavior helps to keep the laminar flow stable, especially in the smooth duct. However, this explanation doesn't work for the turbulent case in the test section because of the ribs [20, 81, 82]. So, the regression method that uses ANOVA to find the fit values of the  $PF$  shown in Table 6 can be modeled as shown in Eq. (13):

$$\begin{aligned}
 PF = & 1.27649 - 0.26333A_{-1} + 0.02382A_0 + 0.23951A_1 + 0.02546B_{-1} \\
 & - 0.00118B_0 - 0.02428B_1 - 0.11482C_{-1} - 0.03288C_0 + 0.14770C_1 \\
 & - 0.00528A_{-1}B_{-1} - 0.00054A_{-1}B_0 + 0.00582A_{-1}B_1 - 0.01126A_0B_{-1} \\
 & + 0.00062A_0B_0 + 0.01063A_0B_1 + 0.01653A_1B_{-1} - 0.00008A_1B_0 \\
 & - 0.01645A_1B_1 - 0.00783A_{-1}C_{-1} + 0.01844A_{-1}C_0 - 0.01061A_{-1}C_1 \\
 & + 0.02481A_0C_{-1} - 0.03711A_0C_0 + 0.01230A_0C_1 - 0.01698A_1C_{-1} \\
 & + 0.01867A_1C_0 - 0.0016A_1C_{-1} - 0.00332B_{-1}C_{-1} - 0.00122B_{-1}C_0 \\
 & + 0.00454B_{-1}C_1 + 0.00047B_0C_{-1} + 0.00002B_0C_0 - 0.00049B_0C_1 \\
 & + 0.00285B_1C_{-1} + 0.00120B_1C_0 - 0.00405B_1C_1
 \end{aligned} \tag{15}$$

R – Sq : 99.96%; R – Sq(adj) : 99.97%; R – Sq(Pred) : 99.54%

Here, the regression behavior in Eq. (15) is the polynomial model for PF that gives us the fitted values compared to the predicted values for this response, which can be seen in Table 7. The model had correlation factors of over 99% for R-sq, R-sq(adj), and R-sq(pred), and the standard deviation was 0.0086447. Accordingly, the ANOVA for mesh size and Reynolds number in Figure 6 has presented an elementary outcome for the best predictive zone. Hence, the integrated configuration of the SPO technique as the final path can be observed in Figure 7. The heat map in Figure 7 shows the distribution of parameters utilized in the current work. Furthermore, it has highlighted the final optimal zone in maroon color at 18, 1600, and triangle duct for the mesh size, Reynolds number, and duct type, respectively. The results of the optimization plot in Figure 7, on the other hand, match the results of this map in Figure 7 at  $D = 0.9830$ , as shown in Eq. (14). Based on the SPO procedures, run 21 in Table 6 is the best level, and run 7 is the worst level based on the PF's minimum output, which can be seen in Figure 8.

As illustrated in Figure 8, the temperature distribution in the optimal and worst cases is contrasting in configuration. In Figure 8, the temperature concentration after each rib is gradually regular compared to Figure 8. This problem is connected to the case of airflow deflection and the streamline velocity in the HRDs for the triangle and square shapes shown in Figure 8, in that order [83–85]. Figure 8 shows that the concentration of airflow deflection, along with the streamlined velocity, went up in a regular pattern after each rib. Figure 8 shows a hybrid ribbed square duct, but it didn't show this behavior. This is because the distribution of airflow deflection and the streamlined velocity wasn't balanced. This variance in the optimal and worst cases is attributed to the increased mesh resolution and Reynolds number in addition to the style of duct employed in this comparison [76–78].

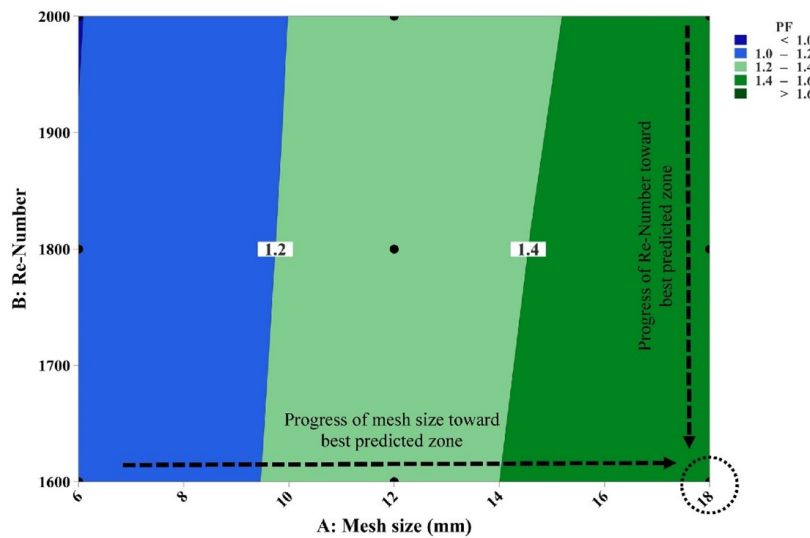


**Figure 6.** Contour plot of PF to mesh size and Reynolds number in HRDs

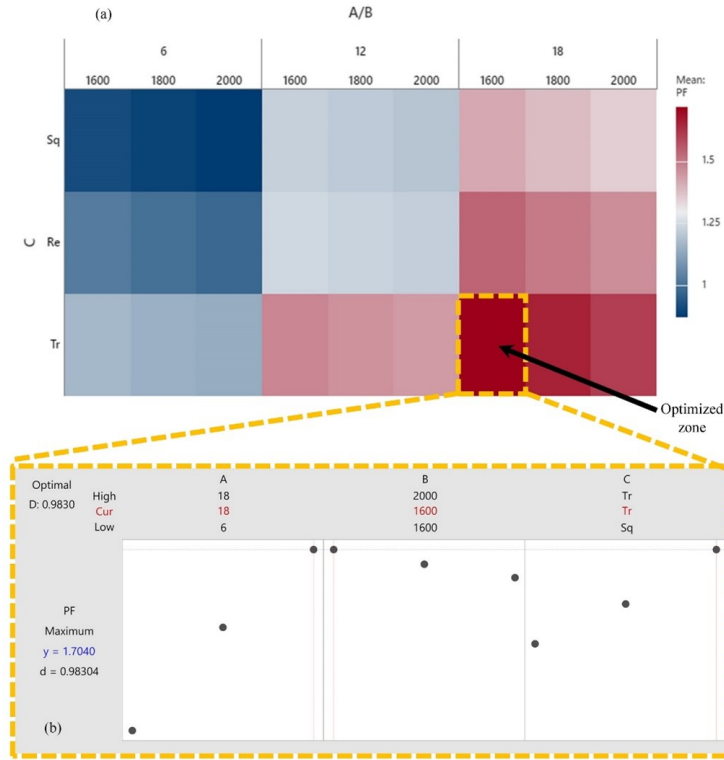


**Figure 7.** Final optimization according to SPO technique. Observed (a) Heat map distribution for PF and parameters; (b) Final destination for SPO and desirability

From these outcomes, the laminar flow at ( $Re = 1600$ ) was a regular inflow at the entrance region of the triangular duct in Figure 8. In addition, the square-ribbed duct possesses the same stable behavior at  $Re = 2000$ , as shown in Figure 8. The main difference between these cases began in the test section, where the ribs changed the flow mechanism to turbulent flow and improved heat transfer, especially at the best run shown in Figure 8. Thus, the role of Reynolds number was observably slightly or stagnant in the ANOVA of the SPO technique. Therefore, the importance of the Reynolds number in ANOVA depending on the P-value and F-value is considered an indicator to specify viscosity model expediency in the simulation. Thus, there has been a need to enhance this simulation by employing an active model for viscosity instead of the laminar model.

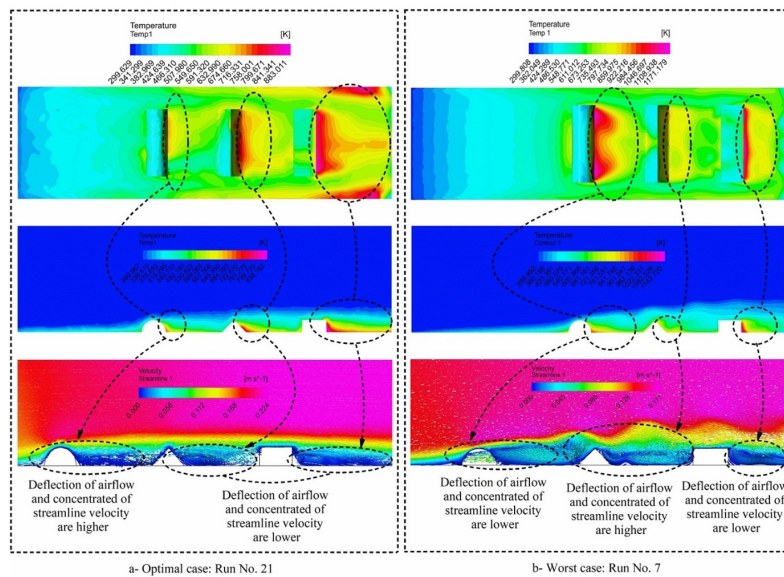


**Figure 8.** Comparison of temperature distribution and streamline velocity of HRDs: (a) Optimal case at run No. 21; (b) Worst case at run No. 7

### 3.2 Outcomes of Investigation Stage

The triangular style of airflow duct induced by the SPO technique was one of the optimal predictive parameters. Therefore, it is essential to investigate one of the experimental studies that adopt this duct style. On the other hand, a comparison of the hybrid and identical ribs to verify the performance of turbulence flow is also needed. ANOVA results in Table 7 show that the laminar viscosity model did not work in the CFD simulation of the ribbed section, as shown by the small effect of Reynolds number on those results. Hence, it is significant to adopt the suitable viscosity model at this stage under the optimal outputs of the previous stage.

Mohammed et al. [38] presented one of these experimental studies that collected the triangular duct shape and the identical style of ribs. One of the cases in this study used  $Re = 1500$  with three ribs adopted to investigate in this stage. The laminar viscosity model has not successfully validated the experimental Nusselt number, as illustrated in Figure 9, where the error ratio approached 55.35%. This fact is attributed to the airflow over a ribbed surface breaking down the laminar boundary layer and becoming turbulent, causing increased friction and a more efficient transfer of heat [86]. Therefore, a laminar viscosity model is unsuitable for accurately simulating fluid flow in ribbed ducts. The zone over 0.2 mm in Figure 9 is powerfully sensitive to the turbulent behavior with the models K- $\epsilon$ -Standard and K- $\epsilon$ -Realizable. These models have achieved 8.83% and 14.16% error ratios, respectively. The deflection of airflow at each rib, according to K- $\epsilon$ -Standard in Figure 9, is more reasonable than the laminar model. Hence, this behavior conforms to the outputs of the ANOVA in Table 7 and Figure 5, where it senses these outputs depending on the significance of the Reynolds number. This investigation has proved the accuracy of the model of K- $\epsilon$ -Standard in the CFD simulation. So, this model can be used to guess how the turbulent flow will spread in three identical and hybrid ribs at 18 mm and 1600 for the mesh size and Reynolds number, in that order, based on the best SPO outputs.

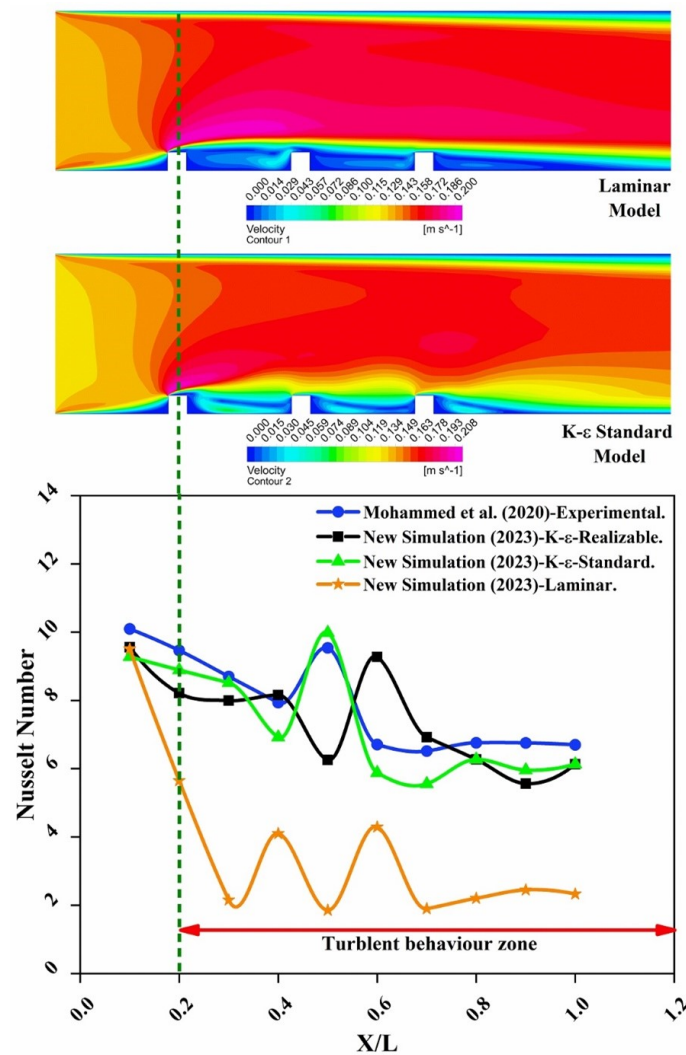


**Figure 9.** Comparison of viscosity models in CFD simulation for identical ribs in triangular duct according to Mohammed et al. [38]



Based on the above, the results of the CFD simulation using the best level of the SPO technique and the K- $\epsilon$ -Standard model were divided into two groups: identical and hybrid styles for the distribution of ribs to find the best performance, as shown in Figure 10. From here, the turbulence intensity of airflow after each rib in the hybrid ribs, as illustrated in Figure 10, is more concentrated than the identical ribs. Hence, the PF for the triangular duct at each style for the rib distribution is 2.0048 and 1.3221 for the hybrid and identical ribs, respectively. Accordingly, this outcome has confirmed the precedence of hybrid ribs compared to the other styles [12–17]. On the other side, the value of this factor is divergent based on the viscosity models employed at the optimum level of hybrid rib style, as demonstrated in Table 8.

The results of this stage showed a useful and important study of how the ribs and viscosity models are distributed in the triangle-shaped duct using the best case scenario of the SPO technique. Therefore, the standard model for k- $\epsilon$  and the hybrid style of ribs adopted in the current study have logically boosted the PF of this duct. However, the turbulence in the test section of hybrid ribs, besides the thermal performance, can be strongly enhanced by increasing the ribs' height [87, 88].

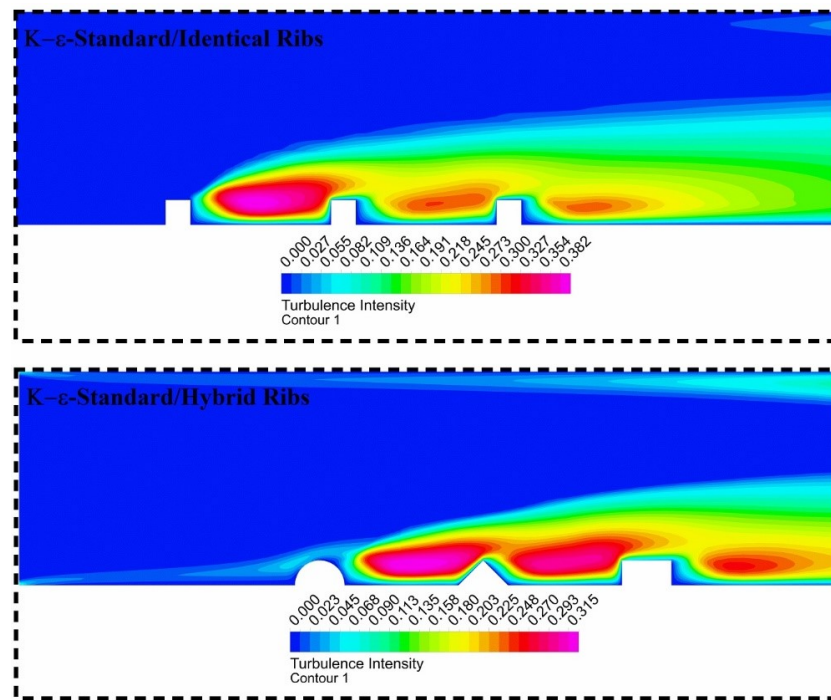


**Figure 10.** Comparison among identical and hybrid style of ribs at  $Re = 1600$  and 18 mm for mesh size in the triangular duct

**Table 8.** PF at optimum level according to viscosity model

Optimum Level According to SPO Technique in HRDs	Viscosity Model	PF-Value
Mesh size = 18, $Re = 1600$ , Triangular duct	Laminar	1.7184
	K- $\epsilon$ -Standard	2.0048

### 3.3 Outcomes of Investigation Stage

Improving the SPO technique for the triangle-shaped duct at 1600 and 18 mm for Reynolds number and mesh size, respectively, as the best level is a very important step to make the turbulence stronger. Finding out that the K- $\epsilon$ -Standard model works better at predicting thermal flow at this important level for each rib in the hybrid style of the ribs distribution shown in subgraph (3-c) of Figure 1 is shown in Figure 10. This is in contrast to the same style. The SSP is deemed the best integration step for reliability to boost the optimal level of the SPO technique by improving the ribs' size for the triangular duct. So, this step includes finding the total chances of the ribs getting taller, reducing these chances using Central Composite Design (CCD), analyzing the results using Response Surface Methodology (RSM), and finally making the design better [89–91].



**Table 9.** PF at optimum level according to viscosity model

Rib Style	Proposed Height (mm)			
Semi-Circle rib	30	40	50	60
Triangular rib	30	40	50	60
Rectangular rib	30	40	50	60

As depicted in Figure 11, the steps of the SSP path were followed depending on the proposed heights over 30 mm to enhance the vortices at the test section [92–94]. These heights for semi-circle, triangular, and rectangular ribs are 30, 40, 50, and 60 mm for each rib, as released in Table 9. So, it can figure out the paths that were predicted by SSP using different PF values based on the parameter parallel chart (PPC) in Figure 11 at each stage. As a final optimization, the final destination of SSP in Figure 11 shows that the best level of SPO was raised by making the rib height 66, 66, and 38.126 mm for semicircular, rectangular, and triangular ribs, respectively, instead of 30 mm for each rib. Because of this, it is clear that the turbulence intensity and PF values change at these increasing heights in the triangular duct, as shown in Table 10 for SSP and CFD.

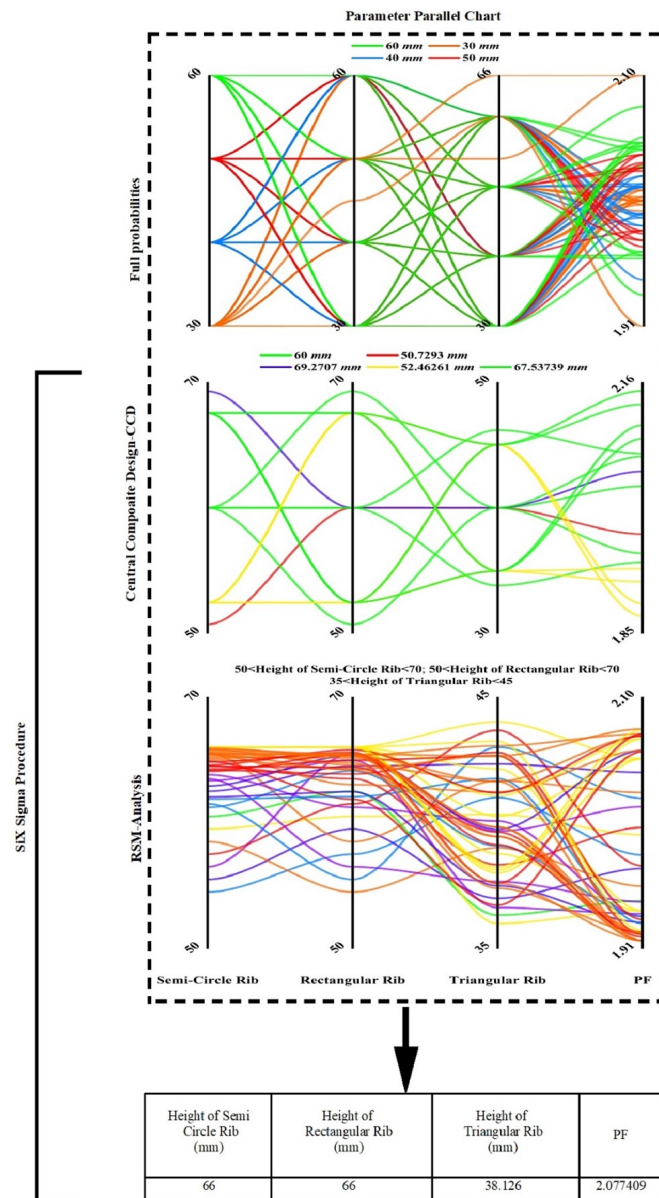


**Figure 11.** SSP to predict the heights for hybrid ribs in the triangular duct at  $Re = 1600$  and 18 mm for mesh size. Observably, the parameter parallel chart according to SSP for each stage is full probabilities, CCD, RSM-Analysis, and final optimization

The way air flows through the triangular duct changes depending on the amount of turbulence shown in Figure 12. This is different for the hybrid ribs at 30 mm in Figure 12 compared to the traditional hybrid ribs at the same height. Hence, the predicted result from CFD simulation is different from the outcome of SSP, as illustrated in Table 9. Hereby, the error ratio between these outcomes for the final optimal responses of PF and turbulence intensity in Table 9 was 1.233% and 0.554%, respectively. Besides, these outcomes achieved in Figure 12 are indicators of enhancement in the thermal performance depending on the path of SSP depicted in Figure 11. So, the turbulence intensity at 30 mm for each rib at the best level of the SPO was 0.042318, as shown in Figure 12. In Figure 12, this value has grown to 0.104431 when the SSP path is used. These outputs refer to an increase in the turbulence intensity up to 146.77%, depending on this enhancement. Accordingly, this enhancement has increased the PF to 4.90%. Hence, the optimal predictive path of SSP has boosted this factor for the triangular duct at the optimum level of the SPO technique.

**Table 10.** PF at optimum level according to viscosity model

Predicted Mechanism	Responses	
	Turbulence Intensity (TI)	Performance Factor (PF)
SSP	0.105010	2.077409
CFD	0.104431	2.103044
%€	0.554	1.233

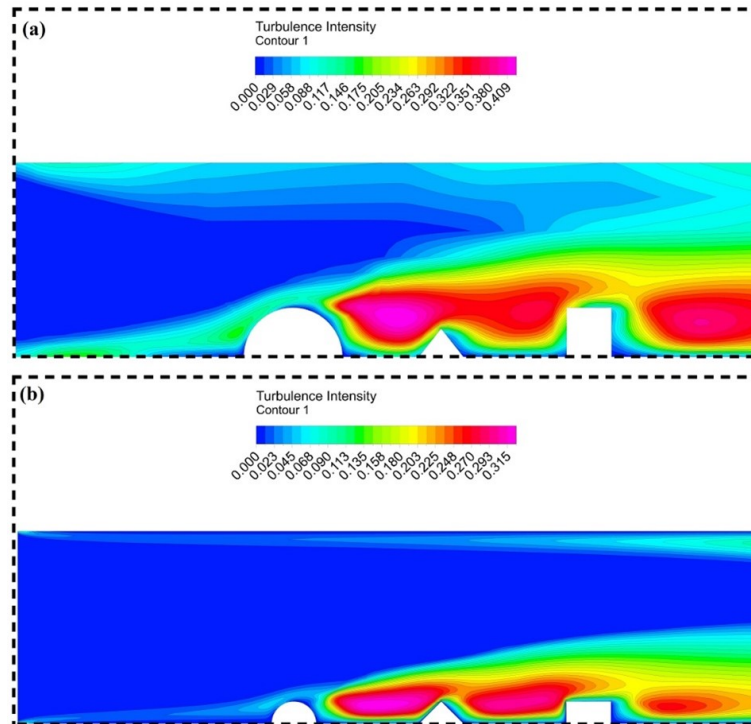


**Figure 12.** Comparison between optimum level of turbulence intensity resulted by SPO at: (a) Enhancement of hybrid ribs heights with SSP; (b) Without enhancement of hybrid ribs at 30 mm for each ribs

#### 4 Conclusions

The enhancement of heat performance in the airflow ducts has constituted an obsession for researchers in this field. Therefore, numerous predictive paths have been explored to enhance this factor. Consequently, this study presented a deep scenario to adopt the best outcome of the PF by employing the mesh size, duct style, and laminar range of the Reynolds number at 1600–2000. Besides, it utilized a hybrid distribution of ribs inside square, rectangular, and triangular ducts. Thus, this study has concluded the following:

(1) At 18, 1600, and triangular duct for mesh size and Reynolds number beside duct style, respectively, represented the optimal outcomes according to the SPO. This optimal level produced the best PF and was equal to 1.7184 at 99.96% and 0.9830 for the correlation factor and desirability function sequentially.

(2) The ANOVA was a successful indicator to sense the illogical behavior of the laminar model of viscosity in the test section, where the model of K- $\epsilon$ -Standard achieved the best investigation compared to other models, including the laminar model.

(3) At the optimal level based on the SPO technique, the hybrid rib distribution was better than the identical style of ribs in the triangular duct. Accordingly, the value of PF with the hybrid rib style was 2.0048 as compared to the performance of the identical distribution.

(4) The predictive PF according to the SSP path was boosted to 2.077409 since the improved ribs' heights were over 30 mm at 66, 66, and 38.126 mm for semi-circle, rectangular, and triangular ribs at the optimal level resulting from the SPO technique. On the other hand, the predictive simulation utilizing CFD has produced 2.103044 for this factor. Therefore, the error ratio of the PF between SSP and CFD was 1.233%. From this point on, this error ratio shows how the SSP path raises the SPO outputs by using these ribs' heights for the triangle hollow tube. Thus, the performance of this enhanced ribbed duct has increased to 4.90%, and this increase led to the growth of turbulence intensity to 146.77%.

The results derived from this investigation underscore the significant enhancement in heat performance achieved in a triangular HRD when employing SPO and SSP techniques. The pivotal contribution of this study lies in the optimized enhancement of laminar flow heat performance through these methodologies. It has been demonstrated that effective stimulation of flow simulation predictions can be realized by adopting these optimization approaches.

Furthermore, the implications of these findings extend beyond the immediate scope of this study. The methodologies and results herein present a promising potential for application in solar technologies, particularly in the solar air heater (SAH) system. The adaptability and effectiveness of the optimized laminar flow in such applications offer fertile ground for future research.

This study's emphasis on optimization methods for flow simulation in triangular HRDs aligns with the current needs for enhancing energy efficiency in solar technologies. The research methodologies employed and the results obtained contribute significantly to the field, offering a foundation for further explorations and practical applications in energy-efficient designs.

In summary, the study provides a comprehensive approach to optimizing laminar flow in non-circular ducts, with a particular focus on triangular HRDs. The integration of SPO and SSP techniques has proven to be effective, paving the way for their application in solar energy systems, such as the SAH system. Future investigations could expand upon these findings, exploring the broader applicability and potential modifications to enhance the performance and efficiency of such systems.

## Acknowledgement

The authors express their heartfelt gratitude and appreciation to the Ministry of Higher Education and Scientific Research, Iraq, for their support. Moreover, they extend their special thanks to the Sustainable Manufacturing and Recycling Technology-Advanced Manufacturing and Materials Centre (SMART-AMMC) at Universiti Tun Hussein Onn Malaysia (UTHM), and the Mechanical Engineering Department at the Faculty of Engineering, University of Kufa, as well as the Engineering Technical College-Najaf/Al-Furat Al-Awsat Technical University (ATU) for their invaluable assistance.

## Data Availability

The data used to support the research findings are available from the corresponding author upon request.

## Conflicts of Interest

The authors declare no conflict of interest.

## References

- [1] M. E. Haque, M. S. Hossain, and H. M. Ali, "Laminar forced convection heat transfer of nanofluids inside non-circular ducts: A review," *Powder Technol.*, vol. 378, pp. 808–830, 2021. <https://doi.org/10.1016/j.powtec.2020.10.042>
- [2] H. Ranjan, A. K. Bharti, M. S. Emani, J. P. Meyer, and S. K. Saha, "New combined heat transfer enhancement techniques used in laminar flow through non-circular ducts," *Appl. Therm. Eng.*, vol. 163, p. 114325, 2019. <https://doi.org/10.1016/j.applthermaleng.2019.114325>
- [3] S. K. Mahato, S. C. Rana, and R. N. Barman, "Heat transfer and fluid flow characteristics within non-circular duct," *IOP Conf. Ser.: Mater. Sci. Eng.*, vol. 1146, no. 1, p. 012013, 2021. <https://doi.org/10.1088/1757-899X/1146/1/012013>
- [4] R. Kumar, Varun, and A. Kumar, "Thermal and fluid dynamic characteristics of flow through triangular cross-sectional duct: A review," *Renew. Sust. Energ. Rev.*, vol. 61, pp. 123–140, 2016. <https://doi.org/10.1016/j.rser.2016.03.011>

- [5] H. F. Oztop, "Effective parameters on second law analysis for semicircular ducts in laminar flow and constant wall heat flux," *Int. Commun. Heat Mass Transf.*, vol. 32, no. 1-2, pp. 266–274, 2005. <https://doi.org/10.1016/j.icheatmasstransfer.2004.05.018>
- [6] A. Z. Şahin, "A second law comparison for optimum shape of duct subjected to constant wall temperature and laminar flow," *Heat Mass Transf.*, vol. 33, no. 5-6, pp. 425–430, 1998. <https://doi.org/10.1007/s002310050210>
- [7] E. B. Ratts and A. G. Raut, "Entropy generation minimization of fully developed internal flow with constant heat flux," *J. Heat Transf.*, vol. 126, no. 4, pp. 656–659, 2004. <https://doi.org/10.1115/1.1777585>
- [8] P. Promvong, W. Changcharoen, S. Kwankaomeng, and C. Thianpong, "Numerical heat transfer study of turbulent square-duct flow through inline V-shaped discrete ribs," *Int. Commun. Heat Mass Transf.*, vol. 38, no. 10, pp. 1392–1399, 2011. <https://doi.org/10.1016/j.icheatmasstransfer.2011.07.014>
- [9] S. Singh, S. Chander, and J. S. Saini, "Heat transfer and friction factor correlations of solar air heater ducts artificially roughened with discrete V-down ribs," *Energy*, vol. 36, no. 8, pp. 5053–5064, 2011. <https://doi.org/10.1016/j.energy.2011.05.052>
- [10] R. Hassanzadeh and N. Tokgoz, "Analysis of heat and fluid flow between parallel plates by inserting triangular cross-section rods in the cross-stream plane," *Appl. Therm. Eng.*, vol. 160, p. 113981, 2019. <https://doi.org/10.1016/j.applthermaleng.2019.113981>
- [11] S. Pourhedayat, S. M. Pesteei, H. E. Ghalinghie, M. Hashemian, and M. A. Ashraf, "Thermal-exergetic behavior of triangular vortex generators through the cylindrical tubes," *Int. J. Heat Mass Transf.*, vol. 151, p. 119406, 2020. <https://doi.org/10.1016/j.ijheatmasstransfer.2020.119406>
- [12] R. Misra, J. Singh, S. K. Jain, S. Faujdar, M. Agrawal, A. Mishra, and P. K. Goyal, "Prediction of behavior of triangular solar air heater duct using V-down rib with multiple gaps and turbulence promoters as artificial roughness: A CFD analysis," *Int. J. Heat Mass Transf.*, vol. 162, p. 120376, 2020. <https://doi.org/10.1016/j.ijheatmasstransfer.2020.120376>
- [13] K. Nidhul, S. Kumar, A. K. Yadav, and S. Anish, "Enhanced thermo-hydraulic performance in a V-ribbed triangular duct solar air heater: CFD and exergy analysis," *Energy*, vol. 200, p. 117448, 2020. <https://doi.org/10.1016/j.energy.2020.117448>
- [14] S. Alfarawi, S. A. Abdel-Moneim, and A. Bodalal, "Experimental investigations of heat transfer enhancement from rectangular duct roughened by hybrid ribs," *Int. J. Thermal Sci.*, vol. 118, pp. 123–138, 2017. <https://doi.org/10.1016/j.ijthermalsci.2017.04.017>
- [15] Karmveer, N. K. Gupta, M. I. H. Siddiqui, D. Dobrotă, T. Alam, M. A. Ali, and J. Orfi, "The effect of roughness in absorbing materials on solar air heater performance," *Materials*, vol. 15, no. 9, p. 3088, 2022. <https://doi.org/10.3390/ma15093088>
- [16] R. S. Gill, V. S. Hans, and R. P. Singh, "Optimization of artificial roughness parameters in a solar air heater duct roughened with hybrid ribs," *Appl. Thermal Eng.*, vol. 191, p. 116871, 2021. <https://doi.org/10.1016/j.applthermaleng.2021.116871>
- [17] N. M. Phu and N. Van Hap, "Performance evaluation of a solar air heater roughened with conic-curve profile ribs based on efficiencies and entropy generation," *Arab. J. Sci. Eng.*, vol. 45, no. 11, pp. 9023–9035, 2020. <https://doi.org/10.1007/s13369-020-04676-3>
- [18] R. Kumar, S. K. Verma, N. K. Gupta, A. Z. Mendiburu, A. Sharma, T. Alam, and S. M. Eldin, "Experimental assessment and modeling of solar air heater with V shape roughness on absorber plate," *Case Stud. Therm. Eng.*, vol. 43, p. 102784, 2023. <https://doi.org/10.1016/j.csite.2023.102784>
- [19] T. Moradi, H. Shahbazian, M. Hoseinalipour, and B. Sunden, "Effects of wavy ribs on vortex generation and thermal-hydraulic performance in a rotating rectangular channel," *Appl. Thermal Eng.*, vol. 222, p. 119952, 2023. <https://doi.org/10.1016/j.applthermaleng.2022.119952>
- [20] S. W. Ahn, "The effects of roughness types on friction factors and heat transfer in roughened rectangular duct," *Int. Commun. Heat Mass Transf.*, vol. 28, no. 7, pp. 933–942, 2001. [https://doi.org/10.1016/S0735-1933\(01\)00297-4](https://doi.org/10.1016/S0735-1933(01)00297-4)
- [21] A. M. E. Momin, J. S. Saini, and S. C. Solanki, "Heat transfer and friction in solar air heater duct with V-shaped rib roughness on absorber plate," *Int. J. Heat Mass Transf.*, vol. 45, no. 16, pp. 3383–3396, 2002. [https://doi.org/10.1016/S0017-9310\(02\)00046-7](https://doi.org/10.1016/S0017-9310(02)00046-7)
- [22] S. Singh, S. Chander, and J. S. Saini, "Thermo-hydraulic performance due to relative roughness pitch in V-down rib with gap in solar air heater duct-comparison with similar rib roughness geometries," *Renew. Sustain. Energy Rev.*, vol. 43, pp. 1159–1166, 2015. <https://doi.org/10.1016/j.rser.2014.11.087>
- [23] M. L. De Bertodano, R. T. Lahey Jr, and O. C. Jones, "Phase distribution in bubbly two-phase flow in vertical ducts," *Int. J. Multiphase Flow*, vol. 20, no. 5, pp. 805–818, 1994. [https://doi.org/10.1016/0301-9322\(94\)90095-7](https://doi.org/10.1016/0301-9322(94)90095-7)
- [24] R. Kamali and A. R. Binesh, "The importance of rib shape effects on the local heat transfer and flow friction

- characteristics of square ducts with ribbed internal surfaces,” *Int. Commun. Heat Mass Transf.*, vol. 35, no. 8, pp. 1032–1040, 2008. <https://doi.org/10.1016/j.icheatmasstransfer.2008.04.012>
- [25] Z. Hafsi, S. Elaoud, and M. Mishra, “A computational modelling of natural gas flow in looped network: Effect of upstream hydrogen injection on the structural integrity of gas pipelines,” *J. Nat. Gas Sci. Eng.*, vol. 64, pp. 107–117, 2019. <https://doi.org/10.1016/j.jngse.2019.01.021>
- [26] G. Vinay, A. Wachs, and J. F. Agassant, “Numerical simulation of weakly compressible Bingham flows: The restart of pipeline flows of waxy crude oils,” *J. Non-Newton. Fluid Mech.*, vol. 136, no. 2-3, pp. 93–105, 2006. <https://doi.org/10.1016/j.jnnfm.2006.03.003>
- [27] M. F. Naccache and P. R. S. Mendes, “Heat transfer to non-Newtonian fluids in laminar flow through rectangular ducts,” *Int. J. Heat Fluid Flow*, vol. 17, no. 6, pp. 613–620, 1996. [https://doi.org/10.1016/S0142-727X\(96\)00062-8](https://doi.org/10.1016/S0142-727X(96)00062-8)
- [28] S. Y. Kim, D. H. Shin, C. S. Kim, G. C. Park, and H. K. Cho, “Flow visualization experiment in a two-side wall heated rectangular duct for turbulence model assessment in natural convection heat transfer,” *Nucl. Eng. Des.*, vol. 341, pp. 284–296, 2019. <https://doi.org/10.1016/j.nucengdes.2018.11.012>
- [29] R. Kumar and S. K. Verma, “Numerical investigation of performance analysis of triangular solar air heater using computational fluid dynamics (CFD),” *IOP Conf. Ser.: Mater. Sci. Eng.*, vol. 1116, no. 1, p. 012047, 2021. <https://iopscience.iop.org/article/10.1088/1757-899X/1116/1/012047>
- [30] L. B. B. Raju, G. R. K. Sastry, S. K. Gugulothu, K. K. Reddy, and B. Deepanraj, “Numerical investigation on fully-developed heat transfer augmentation and friction factor with dimple shaped intrusion and different radius of curvatures on triangular ducts,” *Appl. Therm. Eng.*, vol. 221, p. 119661, 2023. <https://doi.org/10.1016/j.applthermaleng.2022.119661>
- [31] O. Manca, S. Nardini, and D. Ricci, “A numerical study of nanofluid forced convection in ribbed channels,” *Appl. Therm. Eng.*, vol. 37, pp. 280–292, 2012. <https://doi.org/10.1016/j.applthermaleng.2011.11.030>
- [32] H. Soltanipour, P. Choupani, and I. Mirzaee, “Numerical analysis of heat transfer enhancement with the use of  $\gamma$ - $\text{Al}_2\text{O}_3$ /water nanofluid and longitudinal ribs in a curved duct,” *Therm. Sci.*, vol. 16, no. 2, pp. 469–480, 2012. <https://doi.org/10.2298/tsci110719028s>
- [33] H. U. Choi, K. A. Moon, S. B. Kim, and K. H. Choi, “CFD analysis of the heat transfer and fluid flow characteristics using the rectangular rib attached to the fin surface in a solar air heater,” *Sustainability*, vol. 15, no. 6, p. 5382, 2023. <https://doi.org/10.3390/su15065382>
- [34] D. Maynes, B. Webb, J. Crockett, and V. Solovjov, “Analysis of laminar slip-flow thermal transport in microchannels with transverse rib and cavity structured superhydrophobic walls at constant heat flux,” *J. Heat Transf.*, vol. 135, no. 2, p. 021701, 2013. <https://doi.org/10.1115/1.4007429>
- [35] T. S. Ravikumar, S. Seralathan, V. Hariram, and H. K. Guntamadugu, “Numerical studies on heat transfer over a flat plate with triangular rib-groove geometry at laminar flow conditions,” *Defect Diffus. Forum*, vol. 374, pp. 121–130, 2017. <https://doi.org/10.4028/www.scientific.net/DDF.374.121>
- [36] A. Aghanajafi, D. Toghraie, and B. Mehmandoust, “Numerical simulation of laminar forced convection of water-cuo nanofluid inside a triangular duct,” *Physica E: Low-dimens. Syst. Nanostruct.*, vol. 85, pp. 103–108, 2017. <https://doi.org/10.1016/j.physe.2016.08.022>
- [37] R. Kumar, A. Kumar, and V. Goel, “A parametric analysis of rectangular rib roughened triangular duct solar air heater using computational fluid dynamics,” *Sol. Energy*, vol. 157, pp. 1095–1107, 2017. <https://doi.org/10.1016/j.solener.2017.08.071>
- [38] H. H. Mohammed, W. A. Rasheed, N. A. Jabbar, and L. S. Alansari, “The effect of rib size and configuration towards the flow direction of a triangular duct on enhancing heat transfer factors (Part 1: An experimental study),” *J. Mech. Eng. Res. Dev.*, vol. 43, pp. 406–421, 2020.
- [39] W. S. Janna, *Introduction to Fluid Mechanics*. Broken Sound Parkway, New York: CRC Press, 2015.
- [40] R. Kumar, A. Kumar, and V. Goel, “Numerical simulation of flow through equilateral triangular duct under constant wall heat flux boundary condition,” *J. Inst. Eng. India Ser. C*, vol. 98, pp. 313–323, 2017. <https://doi.org/10.1007/s40032-016-0290-5>
- [41] S. V. Patankar, *Numerical Heat Transfer and Fluid Flow*. Broken Sound Parkway, New York: Taylor & Francis, 2018.
- [42] R. Vinuesa, C. Prus, P. Schlatter, and H. M. Nagib, “Convergence of numerical simulations of turbulent wall-bounded flows and mean cross-flow structure of rectangular ducts,” *Meccanica*, vol. 51, pp. 3025–3042, 2016. <https://doi.org/10.1007/s11012-016-0558-0>
- [43] J. A. C. Humphrey, J. H. Whitelaw, and G. Yee, “Turbulent flow in a square duct with strong curvature,” *J. Fluid Mech.*, vol. 103, pp. 443–463, 1981. <https://doi.org/10.1017/S0022112081001419>
- [44] N. Sahiti, A. Lemouedda, D. Stojkovic, F. Durst, and E. Franz, “Performance comparison of pin fin in-duct flow arrays with various pin cross-sections,” *Appl. Therm. Eng.*, vol. 26, no. 11-12, pp. 1176–1192, 2006.

<https://doi.org/10.1016/j.applthermaleng.2005.10.042>

- [45] A. Ashrafizadeh, G. D. Raithby, and G. D. Stubley, "Direct design of ducts," *J. Fluids Eng.*, vol. 125, no. 1, pp. 158–165, 2003. <https://doi.org/10.1115/1.1514201>
- [46] G. Verma and S. Singh, "Computational multiphase iterative solution procedure for thermal performance investigation of phase change material embedded parallel flow solar air heater," *J. Energy Storage*, vol. 39, p. 102642, 2021. <https://doi.org/10.1016/j.est.2021.102642>
- [47] S. Geller, M. Krafczyk, J. Tölke, S. Turek, and J. Hron, "Benchmark computations based on lattice-boltzmann, finite element and finite volume methods for laminar flows," *Comput. Fluids*, vol. 35, no. 8-9, pp. 888–897, 2006. <https://doi.org/10.1016/j.compfluid.2005.08.009>
- [48] W. Jeong and J. Seong, "Comparison of effects on technical variances of computational fluid dynamics (CFD) software based on finite element and finite volume methods," *Int. J. Mech. Sci.*, vol. 78, pp. 19–26, 2014. <https://doi.org/10.1016/j.ijmecsci.2013.10.017>
- [49] F. D. Molina-Aiz, H. Fatnassi, T. Boulard, J. C. Roy, and D. L. Valera, "Comparison of finite element and finite volume methods for simulation of natural ventilation in greenhouses," *Comput. Electron. Agric.*, vol. 72, no. 2, pp. 69–86, 2010. <https://doi.org/10.1016/j.compag.2010.03.002>
- [50] P. M. Knupp, "Algebraic mesh quality metrics," *SIAM J. Sci. Comput.*, vol. 23, no. 1, pp. 193–218, 2001. <https://doi.org/10.1137/S1064827500371499>
- [51] P. M. Knupp, "Algebraic mesh quality metrics for unstructured initial meshes," *Finite Elem. Anal. Des.*, vol. 39, no. 3, pp. 217–241, 2003. [https://doi.org/10.1016/S0168-874X\(02\)00070-7](https://doi.org/10.1016/S0168-874X(02)00070-7)
- [52] S. Scholl, T. Verstraete, F. Duchaine, and L. Gicquel, "Conjugate heat transfer of a rib-roughened internal turbine blade cooling channel using large eddy simulation," *Int. J. Heat Fluid Flow*, vol. 61, pp. 650–664, 2016. <https://doi.org/10.1016/j.ijheatfluidflow.2016.07.009>
- [53] A. H. Theeb and M. A. Mussa, "Numerical investigation on heat transfer enhancement and turbulent flow characteristics in a high aspect ratio rectangular duct roughened by intersecting ribs with inclined ribs," *J. Eng.*, vol. 26, no. 5, pp. 20–37, 2020. <https://doi.org/10.31026/j.eng.2020.05.02>
- [54] G. N. Xie, S. F. Zheng, W. H. Zhang, and B. Sundén, "A numerical study of flow structure and heat transfer in a square channel with ribs combined downstream half-size or same-size ribs," *Appl. Therm. Eng.*, vol. 61, no. 2, pp. 289–300, 2013. <https://doi.org/10.1016/j.applthermaleng.2013.07.054>
- [55] S. Selimli, Z. Recebli, and E. Arcaklioglu, "MHD numerical analyses of hydrodynamically developing laminar liquid lithium duct flow," *Int. J. Hydrog. Energy*, vol. 40, no. 44, pp. 15 358–15 364, 2015. <https://doi.org/10.1016/j.ijhydene.2015.02.020>
- [56] K. A. Pathan, P. S. Dabeer, and S. A. Khan, "Enlarge duct length optimization for suddenly expanded flows," *Adv. Aircr. Spacecr. Sci.*, vol. 7, no. 3, pp. 203–214, 2020. <https://doi.org/10.12989/aas.2020.7.3.203>
- [57] P. Raphe, H. Fellouah, S. Poncet, and M. Ameer, "Ventilation effectiveness of uniform and non-uniform perforated duct diffusers at office room," *Build. Environ.*, vol. 204, p. 108118, 2021. <https://doi.org/10.1016/j.buildenv.2021.108118>
- [58] K. Nidhul, D. Thummar, A. K. Yadav, and S. Anish, "Machine learning approach for optimization and performance prediction of triangular duct solar air heater: A comprehensive review," *Sol. Energy*, vol. 255, pp. 396–415, 2023. <https://doi.org/10.1016/j.solener.2023.02.022>
- [59] A. Z. Aghaie, A. B. Rahimi, and A. Akbarzadeh, "A general optimized geometry of angled ribs for enhancing the thermo-hydraulic behavior of a solar air heater channel—A taguchi approach," *Renew. Energy*, vol. 83, pp. 47–54, 2015. <https://doi.org/10.1016/j.renene.2015.04.016>
- [60] H. M. Kim and K. Y. Kim, "Optimization of three-dimensional angled ribs with RANS analysis of turbulent heat transfer," in *Proc. of the ASME Turbo Expo: Power for Land, Sea, and Air*, vol. 41685, Vienna, Austria, 2004, pp. 375–381. <https://doi.org/10.1115/GT2004-53346>
- [61] G. Huminic and A. Huminic, "A numerical approach on hybrid nanofluid behavior in laminar duct flow with various cross sections," *J. Therm. Anal. Calorim.*, vol. 140, pp. 2097–2110, 2020. <https://doi.org/10.1007/s10973-019-08990-3>
- [62] F. Liu, H. H. Sun, D. X. Zhang, Q. Chen, J. Zhao, and L. Q. Wang, "Optimization of laminar convective heat transfer of oil-in-water nanoemulsion fluids in a toroidal duct," *Int. J. Heat Mass Transf.*, vol. 150, p. 119332, 2020. <https://doi.org/10.1016/j.ijheatmasstransfer.2020.119332>
- [63] Y. T. Yang, H. W. Tang, and C. J. Wong, "Numerical simulation and optimization of turbulent fluids in a three-dimensional angled ribbed channel," *Numer. Heat Transf. Part A: Appl.*, vol. 70, no. 5, pp. 532–545, 2016. <https://doi.org/10.1080/10407782.2016.1173475>
- [64] M. A. Abbas, M. A. Lajis, A. D. Jawad, E. A. Rahim, S. Ahmed, and N. A. Jamil, "Influence of the spark heat on the electrode behavior in powder mixed-EDM environment," *J. Mech. Eng. Sci.*, vol. 13, no. 4, pp. 6125–6143, 2019.



- [65] G. S. A. Ridha, Z. K. Ibrahim, M. A. Abbas, and O. M. Merzah, "Optimum influence of tensile functions on welded parts of AA 2024-T3 produced from friction stir mechanism utilizing air and water," *Period. Eng. Nat. Sci.*, vol. 10, no. 1, pp. 138–150, 2022. <http://dx.doi.org/10.21533/pen.v10i1.2576>
- [66] R. P. Cardoso, J. S. da Motta Reis, D. E. W. Silva, J. G. M. de Barros, and N. A. de Souza Sampaio, "How to perform a simultaneous optimization with several response variables," *Rev. Gest. Secr.*, vol. 14, no. 1, pp. 564–578, 2023. <https://doi.org/10.7769/gesec.v14i1.1536>
- [67] E. Del Castillo, D. C. Montgomery, and D. R. McCarville, "Modified desirability functions for multiple response optimization," *J. Qual. Technol.*, vol. 28, no. 3, pp. 337–345, 1996. <https://doi.org/10.1080/00224065.1996.11979684>
- [68] G. Derringer and R. Suich, "Simultaneous optimization of several response variables," *J. Qual. Technol.*, vol. 12, no. 4, pp. 214–219, 1980. <https://doi.org/10.1080/00224065.1980.11980968>
- [69] A. I. Khuri and M. Conlon, "Simultaneous optimization of multiple responses represented by polynomial regression functions," *Technometrics*, vol. 23, no. 4, pp. 363–375, 1981. <https://doi.org/10.1080/00401706.1981.10487681>
- [70] S. V. Karmare and A. N. Tikekar, "Analysis of fluid flow and heat transfer in a rib grit roughened surface solar air heater using CFD," *Solar Energy*, vol. 84, no. 3, pp. 409–417, 2010. <https://doi.org/10.1016/j.solener.2009.12.011>
- [71] A. M. Darbari, M. A. Alavi, S. R. Saleh, and V. Nejati, "Sensitivity analysis of nanofluid flow over different flat tubes confined between two parallel plates using Taguchi method and statistical analysis of variance," *Int. J. Therm. Sci.*, vol. 173, p. 107428, 2022. <https://doi.org/10.1016/j.ijthermalsci.2021.107428>
- [72] V. S. Korpale, S. P. Deshmukh, C. S. Mathpati, and V. H. Dalvi, "Numerical simulations and optimization of solar air heaters," *Appl. Therm. Eng.*, vol. 180, p. 115744, 2020. <https://doi.org/10.1016/j.applthermaleng.2020.115744>
- [73] H. Q. Tian, B. Tian, D. B. Meng, Q. Xu, and X. Q. Dang, "Influence of cooling and lubrication parameters on robot bone grinding temperature and prediction modeling," *Power Eng. Eng. Thermophys.*, vol. 2, no. 1, pp. 26–41, 2023. <https://doi.org/10.56578/peet.020103>
- [74] H. Parsa, M. Saffar-Avval, and M. R. Hajmohammadi, "3D simulation and parametric optimization of a solar air heater with a novel staggered cuboid baffles," *Int. J. Mech. Sci.*, vol. 205, p. 106607, 2021. <https://doi.org/10.1016/j.ijmecsci.2021.106607>
- [75] L. Xi, L. Xu, J. M. Gao, Z. Zhao, and Y. L. Li, "Numerical analysis and optimization on flow and heat transfer performance of a steam-cooled ribbed channel," *Case Stud. Therm. Eng.*, vol. 28, p. 101442, 2021. <https://doi.org/10.1016/j.csite.2021.101442>
- [76] D. K. Tafti, "Evaluating the role of subgrid stress modeling in a ribbed duct for the internal cooling of turbine blades," *Int. J. Heat Fluid Flow*, vol. 26, no. 1, pp. 92–104, 2005. <https://doi.org/10.1016/j.ijheatfluidflow.2004.07.002>
- [77] H. E. Ahmed, H. A. Mohammed, and M. Z. Yusoff, "Heat transfer enhancement of laminar nanofluids flow in a triangular duct using vortex generator," *Superlatt. Microstruct.*, vol. 52, no. 3, pp. 398–415, 2012. <https://doi.org/10.1016/j.spmi.2012.05.023>
- [78] J. Pérez-García, A. García, R. Herrero-Martín, and J. P. Solano, "Experimental correlations on critical Reynolds numbers and friction factor in tubes with wire-coil inserts in laminar, transitional and low turbulent flow regimes," *Exp. Therm. Fluid Sci.*, vol. 91, pp. 64–79, 2018. <https://doi.org/10.1016/j.expthermflusci.2017.10.003>
- [79] C. W. Leung, T. L. Chan, and S. Chen, "Forced convection and friction in triangular duct with uniformly spaced square ribs on inner surfaces," *Heat Mass Transf.*, vol. 37, no. 1, pp. 19–25, 2001. <https://doi.org/10.1007/s002310000130>
- [80] F. Menasria, M. Zedairia, and A. Moumami, "Numerical study of thermohydraulic performance of solar air heater duct equipped with novel continuous rectangular baffles with high aspect ratio," *Energy*, vol. 133, pp. 593–608, 2017. <https://doi.org/10.1016/j.energy.2017.05.002>
- [81] J. Holgate, A. Skillen, T. Craft, and A. Revell, "A review of embedded large eddy simulation for internal flows," *Arch. Comput. Methods Eng.*, vol. 26, pp. 865–882, 2019. <https://doi.org/10.1007/s11831-018-9272-5>
- [82] J. P. Tsia and J. J. Hwang, "Measurements of heat transfer and fluid flow in a rectangular duct with alternate attached-detached rib-arrays," *Int. J. Heat Mass Transf.*, vol. 42, no. 11, pp. 2071–2083, 1999. [https://doi.org/10.1016/S0017-9310\(98\)00300-7](https://doi.org/10.1016/S0017-9310(98)00300-7)
- [83] S. Kumar, R. Kumar, V. Goel, S. Bhattacharyya, and A. Issakhov, "Exergetic performance estimation for roughened triangular duct used in solar air heaters," *J. Therm. Anal. Calorim.*, vol. 145, pp. 1661–1672, 2021. <https://doi.org/10.1007/s10973-021-10852-w>
- [84] H. Lu and L. Lu, "A numerical study of particle deposition in ribbed duct flow with different rib shapes," *Build.*

*Environ.*, vol. 94, pp. 43–53, 2015. <https://doi.org/10.1016/j.buildenv.2015.07.030>

- [85] H. Togun, S. Hamidatou, H. I. Mohammed, A. M. Abed, A. H. Hasan, R. Z. Homod, A. W. Al-Fatlawi, M. Al-Thamir, and T. Abdulrazzaq, “Numerical simulation on heat transfer augmentation by using innovative hybrid ribs in a forward-facing contracting channel,” *Symmetry*, vol. 15, no. 3, p. 690, 2023. <https://doi.org/10.3390/sym15030690>
- [86] A. Kumar and M. H. Kim, “Thermohydraulic performance of rectangular ducts with different multiple V-rib roughness shapes: A comprehensive review and comparative study,” *Renew. Sustain. Energy Rev.*, vol. 54, pp. 635–652, 2016. <https://doi.org/10.1016/j.rser.2015.10.030>
- [87] S. V. Mahmoodi-Jezeh and B. C. Wang, “Direct numerical simulation of turbulent heat transfer in a square duct with transverse ribs mounted on one wall,” *Int. J. Heat Fluid Flow*, vol. 89, p. 108782, 2021. <https://doi.org/10.1016/j.ijheatfluidflow.2021.108782>
- [88] L. Q. Shui, J. M. Gao, X. J. Shi, and J. Z. Liu, “Effect of duct aspect ratio on heat transfer and friction in steam-cooled ducts with 60° angled rib turbulators,” *Exp. Therm. Fluid Sci.*, vol. 49, pp. 123–134, 2013. <https://doi.org/10.1016/j.expthermflusci.2013.04.010>
- [89] H. V. S. Bhatta, V. Naveenkumar, A. R. Khajamohideen, B. Couturier, and R. Ganesan, “Numerical simulation methodology for robust optimization using six sigma analysis,” *SAE Technical Paper*, 2021. <https://doi.org/10.4271/2021-28-0248>
- [90] D. Chen, Y. X. Wang, R. L. Liu, J. Zhang, and L. J. Qiu, “Reliability analysis of the optimized carrying door frame based on six-sigma,” *J. Phys.: Conf. Ser.*, vol. 1948, no. 1, p. 012125, 2021. <https://doi.org/10.1088/1742-6596/1948/1/012125>
- [91] J. J. Zhu, X. J. Wang, H. G. Zhang, Y. W. Li, R. X. Wang, and Z. P. Qiu, “Six sigma robust design optimization for thermal protection system of hypersonic vehicles based on successive response surface method,” *Chin. J. Aeronaut.*, vol. 32, no. 9, pp. 2095–2108, 2019. <https://doi.org/10.1016/j.cja.2019.04.009>
- [92] S. S. Bhuvad, R. Azad, and A. Lanjewar, “Thermal performance analysis of apex-up discrete arc ribs solar air heater-An experimental study,” *Renew. Energy*, vol. 185, pp. 403–415, 2022. <https://doi.org/10.1016/j.renene.2021.12.037>
- [93] S. Y. Ran, P. Zhang, and Y. Rao, “Numerical study of heat transfer and flow structure over channel surfaces featuring miniature V rib-dimples with various configurations,” *Int. J. Therm. Sci.*, vol. 172, p. 107342, 2022. <https://doi.org/10.1016/j.ijthermalsci.2021.107342>
- [94] P. Zhang, Y. Rao, Y. Xie, and M. H. Zhang, “Turbulent flow structure and heat transfer mechanisms over surface vortex structures of micro V-shaped ribs and dimples,” *Int. J. Heat Mass Transf.*, vol. 178, p. 121611, 2021. <https://doi.org/10.1016/j.ijheatmasstransfer.2021.121611>